RESEARCH ARTICLE

Receiver Function Investigations of Seismic Anisotropy Layering Beneath Southern California

Fansheng Kong[1,2], Stephen S. Gao[2] (ID)**, Kelly H. Liu[2]** (ID)**, Jianguo Song[2,3], Weiwei Ding[1]** (ID)**, Yinxia Fang[1], Aiguo Ruan[1], and Jiabiao Li[1]** (ID)

[1]Key Laboratory of Submarine Geosciences, Second Institute of Oceanography, State Oceanic Administration, Hangzhou, China, [2]Geology and Geophysics Program, Missouri University of Science and Technology, Rolla, MO, USA, [3]School of Geosciences, China University of Petroleum (East China), Qingdao, China

Abstract Seismic azimuthal anisotropy characterized by shear wave splitting analyses using teleseismic *XKS* phases (including *SKS*, *SKKS*, and *PKS*) is widely employed to constrain the deformation field in the Earth's crust and mantle. Due to the near-vertical incidence of the *XKS* arrivals, the resulting splitting parameters (fast polarization orientations and splitting times) have an excellent horizontal but poor vertical resolution, resulting in considerable ambiguities in the geodynamic interpretation of the measurements. Here we use *P*-to-*S* converted phases from the Moho and the 410- (*d*410) and 660-km (*d*660) discontinuities to investigate anisotropy layering beneath Southern California. Similarities between the resulting splitting parameters from the *XKS* and *P*-to-*S* converted phases from the *d*660 suggest that the lower mantle beneath the study area is azimuthally isotropic. Similarly, significant azimuthal anisotropy is not present in the mantle transition zone on the basis of the consistency between the splitting parameters obtained using *P*-to-*S* converted phases from the *d*410 and *d*660. Crustal anisotropy measurements exhibit a mean splitting time of 0.2 ± 0.1 s and mostly NW-SE fast orientations, which are significantly different from the dominantly E-W fast orientations revealed using *XKS* and *P*-to-*S* conversions from the *d*410 and *d*660. Anisotropy measurements using shear waves with different depths of origin suggest that the Earth's upper mantle is the major anisotropic layer beneath Southern California. Additionally, this study demonstrates the effectiveness of applying a set of azimuthal anisotropy analysis techniques to reduce ambiguities in the depth of the source of the observed anisotropy.

1. Introduction

Numerous geophysical investigations have demonstrated that seismic azimuthal anisotropy, which is characterized by the fast polarization orientation (ϕ) and the splitting time (δt), is a near-ubiquitous property of the Earth's crust and mantle especially the upper and lowermost mantle (Long & Silver, 2009; Savage, 1999; Silver, 1996). While anisotropy in the crust is generally regarded as the consequence of shape-preferred orientation of crustal fabrics (Crampin, 1981) or lattice-preferred orientation (LPO) of anisotropic minerals such as mica and amphibole (Tatham et al., 2008), upper mantle anisotropy is mostly attributed to the LPO of olivine (Zhang & Karato, 1995), which is the most abundant mineral in the upper mantle. Under thermal, pressure, and water content conditions that are typical for the upper mantle beneath continents, the dominant LPO for olivine is the A type, which is mainly related to two geodynamic processes. The first is simple shear, which mostly develops in the transitional layer between the lithosphere and asthenosphere (B. B. Yang et al., 2017; Zhang & Karato, 1995) with the observed ϕ being parallel to the flow direction, and the second is vertically coherent deformation of the lithosphere, leading to a ϕ that is perpendicular to the shortening direction (Silver & Chan, 1991). In addition, lithospheric dikes can result in strike-parallel ϕ, as revealed in continental rift zones (Gao et al., 1997, 2010).

A few studies have suggested that beneath some areas, the mantle transition zone (MTZ), which is the region between the 410- and 660-km discontinuities (*d*410 and *d*660, respectively), is also anisotropic, probably as the result of LPO of β spinel in the MTZ (e.g., Fouch & Fischer, 1996; Tong et al., 1994), or metastable olivine in the subducted and horizontally deflected slabs (K. H. Liu et al., 2008). Except for a few isolated areas (e.g., de Wit & Trampert, 2015; A. K. McNamara et al., 2002), the lower mantle between the *d*660 and the top of the D′′ layer has negligible azimuthal anisotropy, probably reflecting the fact that diffusion creep dominates in the lower mantle (Girard et al., 2016; Karato et al., 1995; Meade et al., 1995; Romanowicz & Wenk, 2017).

Some studies indicated that beneath isolated areas, the D″ layer, which is a layer of low seismic velocities with a thickness of a few hundred kilometers above the core-mantle boundary (CMB), possesses significant azimuthal anisotropy that is attributable to either LPO of postperovskite or shape-preferred orientation of structures (Lynner & Long, 2012; Romanowicz & Wenk, 2017).

2. Approaches for Determining the Depth of Anisotropy

Reliably quantifying azimuthal anisotropy and determining which of the five layers, including the crust, upper mantle, MTZ, lower mantle (excluding the D″), and the D″, is anisotropic have been a major task in structural seismological investigations of the Earth's deep interior. While surface wave and P wave anisotropic tomography techniques can provide depth variation of azimuthal anisotropy (e.g., Montagner & Tanimoto, 1991; Wei et al., 2016), the horizontal resolution is low relative to shear wave splitting or receiver function (RF)-based approaches, both of which are the focus of this study.

Previously proposed approaches to estimate the depth of anisotropy can be grouped into three categories, including those (1) based on the splitting parameters of P-to-S converted phases from the CMB, mainly *SKS*, *SKKS*, and *PKS* (collectively called *XKS* hereafter); (2) using the splitting of direct S waves from local events beneath the station; and (3) utilizing RFs from velocity discontinuities at various depths.

2.1. *XKS* Splitting-Based Depth Estimation Approaches

XKS splitting is perhaps the most commonly employed technique in characterizing mantle azimuthal anisotropy. The resulting splitting parameters (ϕ and δt) reflect anisotropy integrated over the entire ray-path from the CMB to the surface on the receiver side (e.g., Long & Silver, 2009; Savage, 1999; Silver & Chan, 1991). A number of approaches have been proposed to estimate the depth of the main contributing source of anisotropy by using the *XKS* splitting parameters (Alsina & Snieder, 1995; Gao et al., 2010; James & Assumpcao, 1996; Long, 2009; Niu & Perez, 2004; Restivo & Helffrich, 2006).

The first approach utilizes the finite frequency effects of *XKS* splitting measurements (Alsina & Snieder, 1995; Monteiller & Chevrot, 2011). The Fresnel zone approach (Alsina & Snieder, 1995) considers the differences in the splitting parameters from different back azimuths (BAZs) recorded by the same station or from the same event recorded by different stations. The major limitations in applying this technique include the required existence of significant lateral variation of the splitting parameters in the vicinity of the stations, the availability of events from either the same or opposite directions, and measurements from closely spaced stations. In addition, simple anisotropy, which is characterized by a single layer of anisotropy with a horizontal axis of symmetry, is required for applying this technique. Furthermore, because of the nonmonochromatic nature of the *XKS* arrivals, the size of the Fresnel zone and thus the depth of anisotropy are dependent on the dominant frequencies of the waveforms (Rumpker & Ryberg, 2000), which may vary from events to events. Another approach relying on the finite frequency effect of *SKS* splittings produces 3-D anisotropic structure using splitting intensity measurements (Favier & Chevrot, 2003; Y. Lin et al., 2014; Monteiller & Chevrot, 2011). The method requires densely spaced stations, and different inversion parameters such as the damping factor can lead to considerably different results, as demonstrated by two recent studies for Southern California, which reached significantly different conclusions about the strength and existence of lithospheric and sublithospheric anisotropy (Y. Lin et al., 2014; Monteiller & Chevrot, 2011).

The second approach is the spatial coherency method (Gao & Liu, 2012; Gao et al., 2010; K. H. Liu & Gao, 2011), which searches for the optimal depth of the centroid of the anisotropic layer by computing a variation factor for each of the candidate depths. The optimal depth corresponds to the minimum variation factor (e.g., see B. B. Yang et al., 2017, for a recent application of this technique to the eastern United States). Similar to the Fresnel zone approach, it requires simple anisotropy, the existence of spatially varying splitting parameters, and a decent azimuthal coverage (K. H. Liu & Gao, 2011).

The third approach utilizes the difference in the splitting parameters obtained using *SKS* and *SKKS* from the same or nearby events, which have nearly identical raypaths in the upper mantle but different in the lower mantle, to investigate anisotropy in the lower mantle (Hall et al., 2004; James & Assumpcao, 1996; Lynner & Long, 2012; Niu & Perez, 2004; Restivo & Helffrich, 2006). This approach requires the coexistence of *SKS* and *SKKS* waves at the same stations and from the same or nearby events, and its application has largely been limited to characterizing the D″ layer. It has been proposed that besides D″ anisotropy, differences in *SKS* and *SKKS* splitting parameters could be caused by other factors, such as frequency dependence as a result

of laterally or vertically variable anisotropic structures (Marson-Pidgeon & Savage, 1997; Rumpker & Silver, 1998), or the interference between *SKS*, *SKKS*, and other phases (Y. Lin et al., 2014).

2.2. Approaches Using Splitting of Shear Waves From Local Earthquakes

Splitting parameters measured using direct *S* waves from earthquakes in the *S* wave window, in which the incidence angle is less than θ (defined as $\sin(\theta) = V_s/V_p$), are used to quantify anisotropy from the focus to the recording station (e.g., Crampin, 1981; Miller & Savage, 2001). This approach has been widely used to study crustal anisotropy, as well as upper mantle and MTZ anisotropy above subduction slabs along which deep earthquakes are frequent (e.g., Fouch & Fischer, 1996; K. H. Liu et al., 2008). Obviously, the application of this technique is limited to seismically active areas.

2.3. RF-Based Approaches

A relatively less frequently used approach for depth estimate is to utilize the splitting of *P*-to-*S* converted phases from velocity discontinuities in the crust and mantle to characterize anisotropy above the discontinuities (Iidaka & Niu, 1998; Kong et al., 2016; Kosarev et al., 1984; McNamara et al., 1994; Vinnik & Montagner, 1996; Wu et al., 2015). Such converted phases are most clearly observed when the original three-component seismograms are source normalized to form RFs. For example, Iidaka and Niu (1998) compared the splittings of *SKS* and *P*-to-*S* conversions from the *d*660 and attributed the difference in the splitting parameters to the contribution of anisotropy in the lower mantle. Another RF-based approach is the fittings of the moveout of the arrivals of the *P*-to-*S* conversions using a sinusoidal function to quantify anisotropy above a discontinuity (e.g., Kong et al., 2016; Liu & Niu, 2012; Rumpker et al., 2014).

One of the disadvantages of this approach is that the signal-to-noise ratio (SNR) on individual RFs is normally low, and thus, it is difficult to obtain reliable splitting parameters using single RFs (Long & Silver, 2009). To enhance the SNR on the radial and transverse components for the purpose of investigating the anisotropy layering, in this study, we stack epicentral distance-corrected RFs in narrow BAZ bands prior to the splitting and moveout analyses, for the purpose of investigating anisotropy layering beneath Southern California and adjacent areas by analyzing RFs associated with the Moho, *d*410, and *d*660, and comparing the results with a uniform *XKS* splitting data set that we recently generated for the contiguous United States (K. H. Liu et al., 2014; B. B. Yang et al., 2016, 2017).

3. Data and Methods

This study covers an area with longitudes ranging from −123° to −114° and latitudes ranging from 31° to 36°, an area that includes the southern part of the Coast Ranges, the southwestern Basin and Range Province, and the adjacent Pacific Plate (Figure 1). The area is chosen for a couple of reasons. First, in terms of the quantity and quality of broadband seismic data, the study area is perhaps unmatched by any other area of similar size in the world. Second, numerous previous *XKS* splitting and crustal anisotropy studies have been conducted in the area (e.g., Y. Li & Malin, 2008; H. Liu et al., 1995; K. H. Liu et al., 2014; Ozalaybey & Savage, 1995; Savage et al., 1990; Savage & Silver, 1993), and results from these studies can be readily compared with measurements from this study.

3.1. Data

The teleseismic data used for the study were recorded over the period of early 1988 to late 2017 by the stations shown in Figure 1 and are archived at the Incorporated Research Institutions for Seismology Data Management Center. All the requested data are from teleseismic events within the epicentral distance range of 32–98° and with a cutoff magnitude of M_c, which is defined as $M_c = 5.2 + (\Delta - 30.0)/(180.0 - 30.0) - D/700.0$, where Δ represents the epicentral distance in degree, and D is the event depth in kilometers (Liu & Gao, 2010).

The requested seismograms are band-pass filtered in the frequency band of 0.08–0.8 Hz prior to computing RFs from the Moho and 0.02–0.2 Hz before computing RFs from the deeper discontinuities (*d*410 and *d*660). Seismograms with an SNR larger than 3.0 on the vertical component are converted to radial and transverse RFs using the water-level deconvolution method (Ammon, 1991). The SNR is defined here as $SNR = \max |A_s|/|\bar{A}_n|$, where $\max |A_s|$ represents the maximum absolute value of a 20-s-long time window of $(T_P - 8 \text{ s}, T_P + 12 \text{ s})$ centered at the predicted arrival time of the first *P* wave (T_P) computed using the IASP91 standard Earth model (Kennett & Engdahl, 1991), and $|\bar{A}_n|$ denotes the background noise calculated as the mean absolute value on the seismogram in the time window of $(T_P - 20 \text{ s}, T_P - 10 \text{ s})$. In addition, two SNR-based procedures are applied
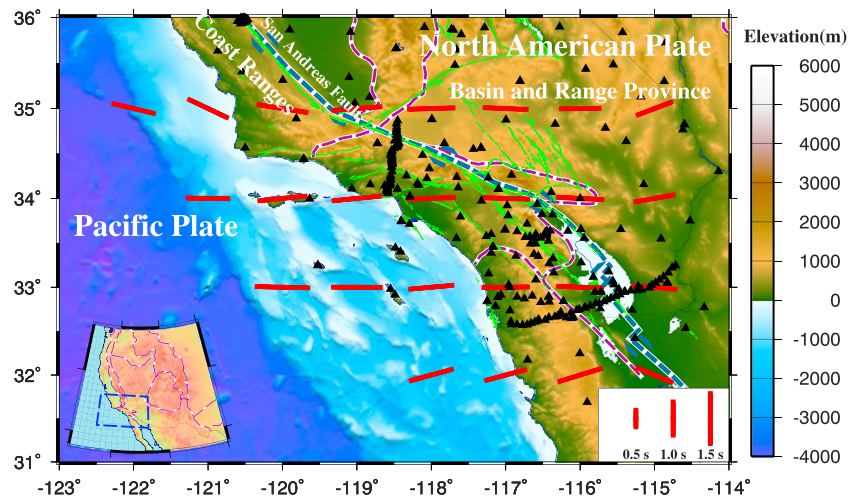
Figure 1. A topographic map showing major tectonic boundaries (purple dashed lines) and active faults (green lines) in Southern California and adjacent areas. The triangles represent the seismic stations used in the study, and the blue dashed line is the San Andreas Fault. The red bars show the averaged *XKS* splitting results of individual measurements (Liu et al., 2014) in radius = 1° bins based on the ray-piercing location at 200-km depth, with the length of the bars being proportional to the splitting time. The inset map shows the study area.

to reject RFs with strong noise before the *P* wave arrival and those with abnormally large arrivals in the *P* wave coda (Gao & Liu, 2014). A total of 77,575 pairs of radial and transverse RFs from 4,715 events (Figure 2) recorded by 319 broadband stations (Figure 1) are used to constrain crustal anisotropy for the study. The number of RFs used for measuring anisotropy above the *d*410 and *d*660 is 70,902.
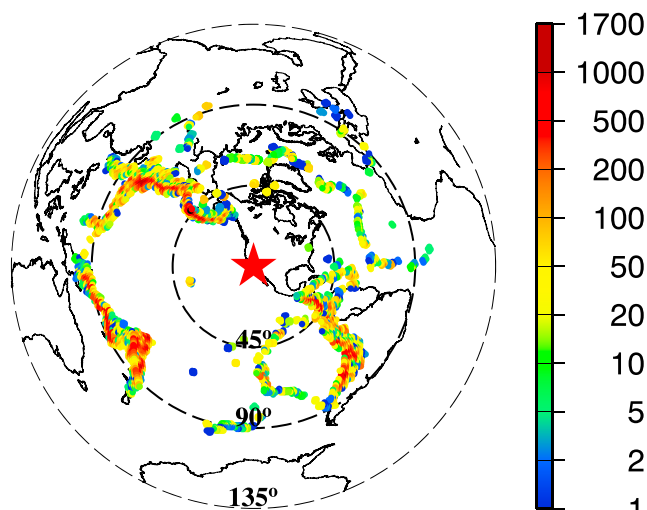
3.2. Moveout Correction and Stacking

To correct the ray parameter dependence of the moveout of the *Pds* phase, which is the *P*-to-*S* conversion from a velocity discontinuity including the Moho (*Pms*), *d*410 (P410s), and *d*660 (P660s), we first calculate the time shift for each of the samples in the RFs relative to the time of the corresponding sample of a reference RF with a ray parameter of 4.4 s per degree, which is approximately the *P* wave ray parameter for a surface event at a distance of 100°. The moveout difference related to the different ray parameters is then corrected by shifting each point on the RFs by the calculated time difference.
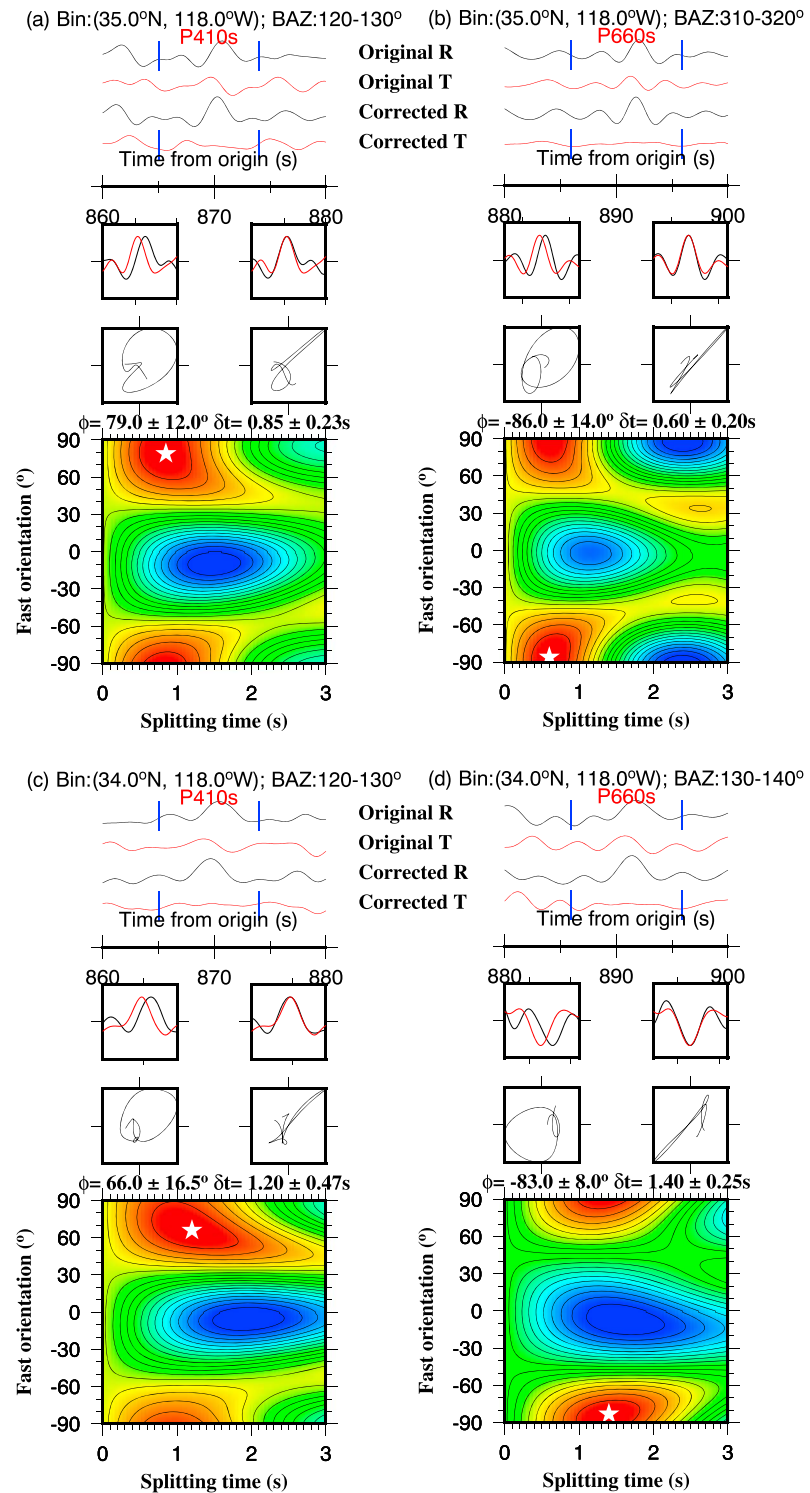

Figure 2. An azimuthal equidistant projection map showing the global distribution of the events used in the study. The color represents the number of receiver functions contributed by events in the circles with a radius of 1°.

For enhancing the SNR of the *Pds* arrivals on the radial and transverse components, the moveout corrected RFs are grouped into 1° circular bins based on the coordinates of the ray-piercing point at the depth of the discontinuity (Moho, *d*410, or *d*660) in the IASP91 Earth model. The distance between the centers of neighboring bins is set as 1° as well, leading to a 39% overlap between any two neighboring bins. All the radial and transverse RFs belonging to the same bin are ray parameter corrected, and those in the same 10° BAZ band are stacked for anisotropy analyses.

3.3. Measuring *Pds* Splitting Parameters

The calculation for the splitting parameters using the stacked RFs is based on the transverse energy minimization method (Silver & Chan, 1991), which computes the optimal pair of splitting parameters that can best remove the energy on the corrected transverse component. The resulting shear wave splitting measurements are initially ranked automatically based on the SNR on the original and corrected radial and transverse RFs with a rank of A (good), B (fair), C (bad), and N (null; Liu & Gao, 2013). Then all of the splitting measurements are manually checked, and if necessary, the time window, the filtering parameters, and the ranking are adjusted. Only those with a rank of A or B are used in the discussion.

Figure 3. Examples of *P*-to-*S* conversion splitting measurements using the P410s (left panels) and P660s (right panels) for the bin centered at (a, b) 35.0°N and 118°W, and (c, d) 34.0°N and 118°W. For each plot, the panels from the top to bottom illustrate the original and corrected radial and transverse components, original and corrected fast (red) and slow (black) components, original and corrected particle motion patterns, and the residual energy function, which represents the energy on the corrected transverse component. The optimal pair of splitting parameters (white star) corresponds to the minimum value on the contour map. BAZ = back azimuth.
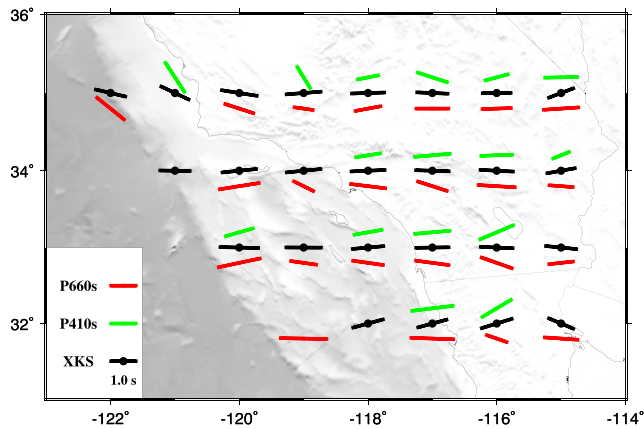
Figure 4. Resulting P410s (green bars) and P660s (red bars) splitting parameters from this study, and *XKS* splitting parameters (black bars) from K. H. Liu et al. (2014). The three types of measurements are shifted along the N-S direction for clarity. The dots represent the center of the circular bins.

3.4. Fitting of Sinusoidal Moveout of *P*-to-*S* Conversions

Systematic azimuthal variations of *Pds* moveout on the radial RFs relative to the first *P* arrival can be utilized to obtain the anisotropy parameters by fitting the sinusoidal moveout of the *Pds* with respect to the BAZ (Liu & Niu, 2012; Rumpker et al., 2014). When a shear wave travels through an anisotropic layer with a horizontal axis of symmetry, the arrival times of the *Pds* relative to the direct *P* arrival on the radial RFs exhibit systematic variations with respect to the BAZ of the events, that is,

$$t = t_0 + \Delta t = t_0 - \frac{\delta t}{2} \cos[2(\alpha - \phi)], \qquad (1)$$

where t_0 is the arrival time when no anisotropy exists, Δt represents the offset of arrival time that is accounted by anisotropy along the raypath, ϕ and δt are the equivalent fast orientation and splitting delay time, respectively, and α stands for the BAZ of the events. The splitting parameters (ϕ and δt) can be obtained by fitting the *Pds* moveout with respect to the BAZ based on a nonlinear least squares fitting procedure (Press et al., 1992). As discussed below, the 180° periodicity shown in the observed RFs suggests that the study area is dominated by a horizontal symmetry axis for both the crust and upper mantle. In order to quantify the uncertainties of the resulting anisotropy measurements, the bootstrap resampling procedure (Efron & Tibshirani, 1986; Press et al., 1992) is applied to calculate the splitting parameters 10 times for each bin.

4. Results

4.1. Results From Splitting of P410s and P660s

Figure 3 shows examples of the splitting analysis using the P410s and P660s phases. While the SNR for the *Pds* phases is admittedly lower than *XKS*, which leads to large uncertainties, the reliability of the resulting splitting parameters is reasonably high based on the decent match between the resulting fast and slow components, as well as the robustness of the minimum value point on the energy contour plot. In general, the P660s has a greater amplitude than P410s in the study area (e.g., Figure 7 in Gao & Liu, 2014) and consequently, more splitting measurements from the former are obtained. The number of bins with reliable splitting parameters is 16 for the P410s and 23 for the P660s (Figure 4 and Table 1).

For the P410s, the resulting fast orientations range from 59° to 149° with a circular mean value (Fisher, 1995) of 83.2 ±22.3°, and the splitting times are between 0.7 and 1.65 s with a simple mean of 1.24 ± 0.27 s. The corresponding numbers for the P660s are 78–129°, 96.0 ± 15.1°, 0.75–1.85 s, and 1.24 ± 0.33 s. The mean splitting parameters obtained using the P410s and P660s for the entire study area are 92.1 ± 18.7° for ϕ and 1.24 ± 0.31 for δt. In comparison, the splitting parameters from *XKS* for the same area are 87.8 ± 17.3° and 1.28 ± 0.36 s (K. H. Liu et al., 2014). The mean *XKS* splitting parameters for each of the bins are computed by averaging the individual-event splitting parameters in K. H. Liu et al. (2014) obtained using the minimization of transverse energy approach (Silver & Chan, 1991). While the bin averages can also be obtained using the multievent stacking procedure (Wolfe & Silver, 1998), a recent study using both synthetic and recorded data suggested that the Wolfe and Silver (1998) approach leads to statistically identical fast orientations but has the tendency of underestimating the splitting times (Kong et al., 2015). In spite of the noticeable inconsistencies in a few bins, which are most likely the results of the low *SNR* of the *Pds* arrivals, no systematic and statistically significant discrepancies exist among the splitting parameters obtained from the P410s, P660s, and *XKS*.

4.2. Results From Sinusoidal Fitting of P410s and P660s Moveouts

We next attempt to obtain the equivalent splitting parameters by fitting the back azimuthal variations of moveouts of the P410s and P660s using the sinusoidal function (equation (1)). While in an ideal situation, the azimuthal coverage of the RFs in each of the bins is sufficient to result in reliable splitting parameters, visual checking of the azimuthal distribution of the RFs found that the BAZ coverage is inadequate for the vast majority of the bins. Therefore, we combine all the RFs recorded by all stations in the study area and divide them into 36 BAZ bands with a width of 10° prior to performing the moveout analysis, for the purpose of obtaining an averaged pair of splitting parameters for the entire study area. Only BAZ bands with 50 or more RFs are used in the fitting.

Table 1
Bin-Averaged Anisotropy Measurements From XKS Splitting, Splitting of P410s and P660s, and Sinusoidal Moveouts of Pms

Bin	ϕ_{XKS} (°)	δt_{XKS} (s)	ϕ_{P660s}	δt_{P660s}	ϕ_{P410s}	δt_{P410s}	ϕ_{Pms}	δt_{Pms}
N32W119	—	—	91.00 ± 5.5	1.85 ± 0.35	—	—	—	—
N32W118	74.56 ± 6.4	1.25 ± 0.30	—	—	—	—	—	—
N32W117	74.85 ± 13.9	1.19 ± 0.37	92.00 ± 1.0	1.70 ± 0.07	83.00 ± 10.0	1.65 ± 0.50	—	—
N32W116	72.80 ± 22.7	1.27 ± 0.44	109.00 ± 17.5	0.85 ± 0.35	59.00 ± 11.0	1.35 ± 0.57	142.93 ± 4.8	0.34 ± 0.05
N32W115	112.97 ± 22.8	1.07 ± 0.39	94.00 ± 2.0	1.33 ± 0.39	—	—	—	—
N33W120	91.33 ± 6.3	1.52 ± 0.28	78.00 ± 2.0	1.70 ± 0.15	74.00 ± 15.5	1.15 ± 0.43	—	—
N33W119	90.29 ± 12.4	1.40 ± 0.27	98.00 ± 5.0	1.03 ± 0.25	—	—	—	—
N33W118	84.93 ± 13.5	1.25 ± 0.31	97.99 ± 7.2	1.23 ± 0.39	80.00 ± 15.3	1.12 ± 0.04	—	—
N33W117	89.22 ± 14.3	1.31 ± 0.37	97.59 ± 9.5	1.33 ± 0.14	84.94 ± 12.3	1.41 ± 0.28	151.13 ± 4.8	0.21 ± 0.02
N33W116	92.45 ± 16.5	1.30 ± 0.39	109.50 ± 9.5	1.30 ± 0.07	67.00 ± 25.6	1.45 ± 0.07	135.80 ± 4.2	0.14 ± 0.02
N33W115	95.67 ± 24.0	1.23 ± 0.36	83.67 ± 6.1	0.97 ± 0.15	—	—	66.15 ± 5.4	0.13 ± 0.01
N34W121	90.96 ± 6.5	1.20 ± 0.23	—	—	—	—	—	—
N34W120	84.28 ± 18.7	1.37 ± 0.28	81.00 ± 3.0	1.60 ± 0.17	—	—	—	—
N34W119	84.35 ± 13.3	1.38 ± 0.30	116.50 ± 11.6	0.88 ± 0.11	—	—	—	—
N34W118	87.55 ± 13.1	1.34 ± 0.31	97.00 ± 8.0	1.40 ± 0.25	81.00 ± 15.3	1.00 ± 0.28	—	—
N34W117	91.82 ± 12.9	1.32 ± 0.37	108.00 ± 2.0	1.23 ± 0.53	85.00 ± 1.0	1.42 ± 0.18	141.57 ± 3.7	0.27 ± 0.03
N34W116	92.90 ± 13.3	1.32 ± 0.39	93.50 ± 14.8	1.47 ± 0.11	88.00 ± 12.0	1.25 ± 0.35	107.31 ± 2.1	0.17 ± 0.02
N34W115	79.75 ± 22.6	1.14 ± 0.40	94.29 ± 28.2	0.95 ± 0.39	68.00 ± 18.0	0.70 ± 0.25	94.45 ± 5.5	0.05 ± 0.02
N35W122	103.39 ± 21.7	1.23 ± 0.29	129.00 ± 4.5	1.40 ± 0.18	—	—	—	—
N35W121	115.43 ± 19.5	1.23 ± 0.31	—	—	147.00 ± 5.5	1.40 ± 0.27	—	—
N35W120	99.02 ± 18.0	1.43 ± 0.38	108.00 ± 7.0	1.20 ± 0.25	—	—	—	—
N35W119	85.56 ± 15.3	1.38 ± 0.32	98.00 ± 3.5	0.75 ± 0.10	149.00 ± 4.0	1.00 ± 0.10	—	—
N35W118	88.26 ± 13.8	1.31 ± 0.32	79.50 ± 14.8	1.03 ± 0.60	79.00 ± 12.0	0.85 ± 0.23	142.67 ± 1.2	0.40 ± 0.02
N35W117	92.47 ± 12.7	1.23 ± 0.31	90.00 ± 9.5	1.30 ± 0.40	108.00 ± 12.5	1.25 ± 0.38	134.07 ± 5.2	0.19 ± 0.04
N35W116	89.20 ± 15.7	1.14 ± 0.34	88.00 ± 17.0	1.15 ± 0.40	75.00 ± 20.0	0.95 ± 0.48	29.63 ± 30.8	0.06 ± 0.04
N35W115	69.07 ± 22.4	1.05 ± 0.33	86.15 ± 17.1	1.40 ± 0.20	89.00 ± 10.0	1.30 ± 0.30	140.09 ± 6.0	0.10 ± 0.01

Both the P410s and P660s demonstrate clear sinusoidal moveouts (Figures 5a and 5b), leading to well-constrained mean splitting parameters of (98.4 ± 2.0°, 0.83 ± 0.09 s) for the P410s and (104.1 ± 6.5°, 0.82 ± 0.17 s) for the P660s. To verify the results, we generate synthetic RFs based on Rumpker et al. (2014) using a set of splitting parameters similar to the above mean values. The azimuthal variation of the *Pds* moveouts agrees well with the observed ones (Figure 5). While in principle lateral velocity heterogeneities above a discontinuity and its depth variation can affect the moveout of the *Pds* arrivals, seismic tomography and RF studies (e.g., Burdick et al., 2017; Gao & Liu, 2014) suggest that both the mantle velocities and MTZ depths are quite uniform across the study area.

4.3. Crustal Anisotropy Measurements
We visually check the azimuthal variation of the *Pms* phase for each of the bins and find that 11 of the bins have an adequate BAZ coverage for measuring crustal anisotropy. Figure 6 shows the RFs for one of the bins, in which periodic azimuthal variations of *Pms* arrival times are observed. The resulting fast orientations of crustal anisotropy (Figure 7 and Table 1) for stations with large (≥ 0.15 s) δt values are dominantly NW-SE, consistent with the strike of the nearby strike-slip faults. The δt measurements, which range from 0.05 to 0.4 s with an average of 0.19 ± 0.11 s, are larger at stations closer to the San Andreas Fault.

5. Discussion
### 5.1. Absence of Significant Azimuthal Anisotropy in the Lower Mantle and MTZ
The similarity between the splitting parameters obtained using *XKS* and P660s (Figure 4) indicates that the lower mantle, which accounts for two thirds of the total mantle volume, is statistically azimuthally isotropic beneath the study area. The same conclusion can be made for the MTZ based on the general agreement
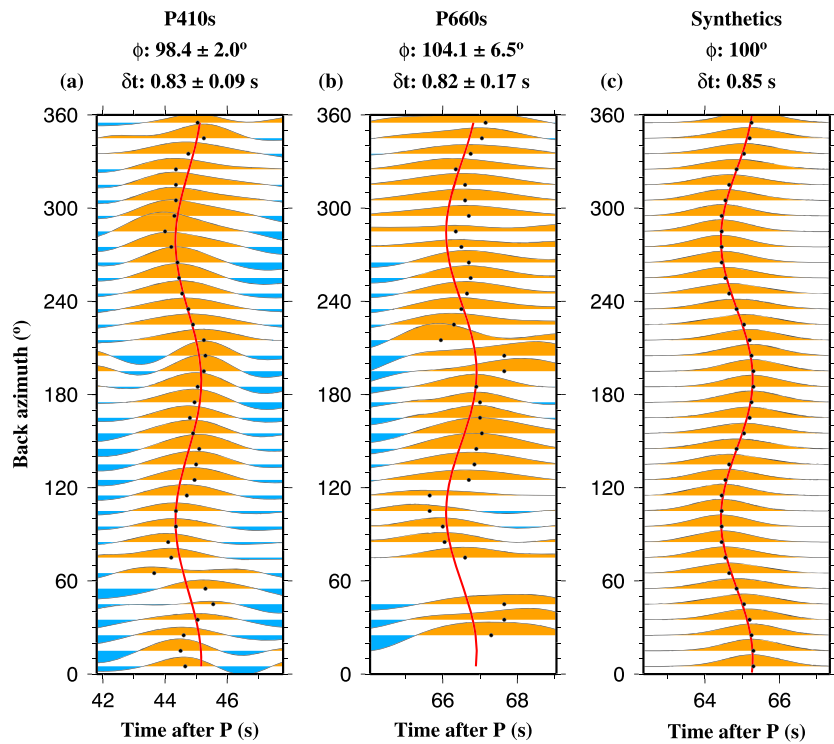
Figure 5. (a) Band-averaged receiver functions recorded by all the stations shown in Figure 1 plotted against the back azimuth. The black dots mark the peak of the P410s, and the red line represents the best fitting curve calculated based on equation (1) using the optimal pair of splitting parameters. (b) Same as Figure 5a but for the P660s. (c) Same as Figure 5b but using synthetic seismic data with a pair of splitting parameters of 100° and 0.85 s.
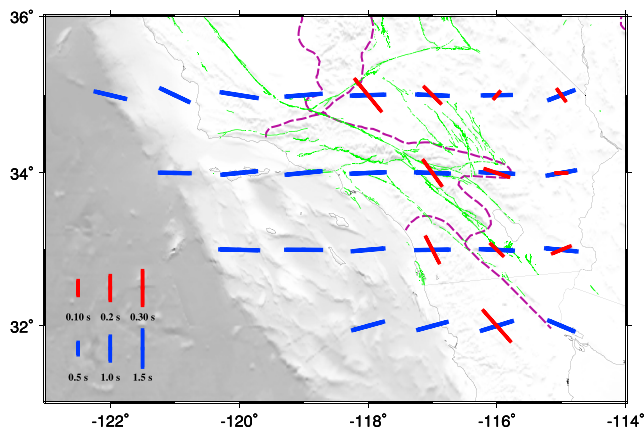
between the splitting parameters obtained using the P660s and P410s, although the two show some differences at a few bins mostly located at the northwestern corner of the study area (Figure 4).

Some previous studies have reported significant anisotropy in the MTZ (e.g., Chen & Brudzinski, 2003; Karato, 1998; K. H. Liu et al., 2008; Vinnik & Montagner, 1996). Those areas are mostly occupied by recently subducted oceanic slabs. One of the anisotropy generating mechanism in the MTZ is metastable olivine in the cold center of the oceanic slab (K. H. Liu et al., 2008; Schubert et al., 2001). The lack of anisotropy in the MTZ beneath
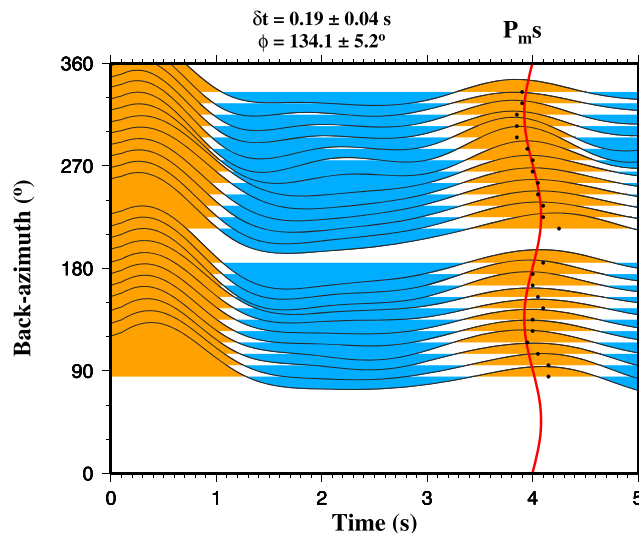
Figure 6. Same as Figure 5a but for the *Pms* receiver functions recorded by stations in the 1° radius bin centered at (35°N, 117°W).

Figure 7. Crustal anisotropy measurements (red bars) obtained using the *Pms* phase and bin-averaged *XKS* splitting parameters (blue bars). Green lines are active faults, and dashed purple lines are tectonic unit boundaries. Note the different scales for the splitting times between the *Pms* and *XKS* results (see legend).

Southern California suggests the absence of cold slabs in the MTZ, a conclusion that is consistent with seismic tomography and RF studies (e.g., Burdick et al., 2017; Gao & Liu, 2014).

Azimuthal anisotropy is observed at a few locations in the D″ layer (e.g., Lynner & Long, 2012; Romanowicz & Wenk, 2017), mostly along the boundaries of large-scale low-velocity anomalies in the lowermost mantle. The lack of lower mantle azimuthal anisotropy beneath this area is consistent with the observation that the D″ layer is largely azimuthally isotropic except for a few isolated areas.

5.2. Crustal and Upper Mantle Anisotropy

The consistencies in the resulting *XKS*, P660s, and P410s anisotropy measurements suggest that anisotropy revealed using the *XKS* phases is mostly located above the *d*410, that is, in the upper mantle and crust. The contribution of the crust to the observed *XKS* splitting is small, as suggested by the large contrast between the splitting times from the *Pms* and *XKS* phases (0.19 versus 1.28 s on average). The fast orientations from the two phases are different at most of the bins, which would lead to azimuthal dependence of the *XKS* splitting parameters over a narrow BAZ band in the modulo-90° domain (Silver & Savage, 1994). If a disproportionally large number of *XKS* events are in the narrow BAZ band, station- or bin-averaged *XKS* splitting parameters cannot objectively reflect the true anisotropy property. Otherwise, averaged parameters are sufficient to represent the anisotropic characteristics, primarily because of the large difference between the *Pms* and *XKS* splitting times.

The resulting fast orientations of crustal anisotropy are in general agreement with those obtained by recent crustal anisotropy studies using RFs (e.g., Porter et al., 2011; Schulte-Pelkum & Mahan, 2014), surface wave tomography (F. Lin et al., 2009), and splitting of shear waves from local earthquakes (e.g., Z. Li & Peng, 2017; Z. Yang et al., 2011). Areas close to major strike-slip faults show NW-SE oriented φ values, which are consistent with fault strike and can be attributed to fluid-filled fractures in the upper crust associated with the numerous strike-slip faults in the study area including the San Andreas Fault system (Crampin, 1981; Z. Li & Peng, 2017), and shear-deformed schists in the lower crust (Porter et al., 2011; Schulte-Pelkum & Mahan, 2014). Detailed discussions about crustal anisotropy in the study area can be found in several recent crustal anisotropy studies that have a much higher lateral resolution than what is used (1°) in this study (Z. Li & Peng, 2017; F. Lin et al., 2009; Porter et al., 2011; Schulte-Pelkum & Mahan, 2014).

Comparison of the measurements using *P*-to-*S* converted phases from the four discontinuities systematically confirms the observation that the upper mantle is the most anisotropic layer, a conclusion that has been reached by surface wave tomography (e.g., Tanimoto & Anderson, 1984), body wave tomography (Huang & Zhao, 2013), overlapping Fresnel zone analysis (Alsina & Snieder, 1995), finite frequency *XKS* tomography (Y. Lin et al., 2014; Monteiller & Chevrot, 2011), and spatial coherency analysis of *XKS* splitting parameters (Gao & Liu, 2012). Such observations are consistent with results from mineral physics experiments, which suggest that concentration of azimuthal anisotropy in the upper mantle is mostly due to the pervasive presence of dislocation creep of olivine crystals under simple shear (Zhang & Karato, 1995). Diffusion creep, which is the dominant form of deformation in the MTZ and lower mantle, is incapable of producing large LPO. This explains the lack of azimuthal anisotropy beneath the *d*410 (Karato et al., 1995).

6. Conclusions

Azimuthal anisotropy measurements obtained using *P*-to-*S* converted phases from four seismic discontinuities, that is, the CMB, *d*660, *d*410, and the Moho, are utilized to investigate anisotropy layering beneath Southern California. The consistency of the anisotropy measurements between splitting parameters from the *XKS* and P660s indicates that the lower mantle beneath the study area is azimuthally isotropic. Similarly, an isotropic MTZ is inferred based on the similarity of the resulting splitting parameters from the P410s and P660s. The fast orientations of crustal anisotropy from the *Pms* phase are different from those obtained from the deeper discontinuities and are mostly parallel to strike-slip faults in the area. On average the crustal splitting times are about 15% of those obtained using the *XKS* phases. This study systematically compares splitting

parameters from all the major discontinuities in the top 2,900 km of the Earth and provides a firm example to demonstrate that the upper mantle possesses the strongest azimuthal anisotropy, due to the pervasive presence of dislocation creep of olivine under simple shear.

References

Alsina, D., & Snieder, R. (1995). Small-scale sublithospheric continental mantle deformation: Constraints from *SKS* splitting observations. *Geophysical Journal International*, *123*, 431–448. https://doi.org/10.1111/j.1365-246x.1995.tb06864.x

Ammon, C. J. (1991). The isolation of receiver effects from teleseismic *P* waveforms. *Bulletin of the Seismological Society of America*, *81*, 2504–2510.

Burdick, S., Vernon, F. L., Martynov, V., Eakins, J., Cox, T., Tytell, J., et al. (2017). Model update, May 2016: Upper-mantle heterogeneity beneath North America from travel-time tomography with global and USArray data. *Seismological Research Letters*, *88*, 319–325. https://doi.org/10.1785/0220160186

Chen, W., & Brudzinski, M. R. (2003). Seismic anisotropy in the mantle transition zone beneath Fiji-Tonga. *Geophysical Research Letters*, *30*(13), 1682. https://doi.org/10.1029/2002GL016330

Crampin, S. (1981). A review of wave motion in anisotropic and cracked elastic-media. *Wave Motion*, *3*, 343–391. https://doi.org/10.1016/0165-2125(81)90026-3

de Wit, R. W. L., & Trampert, J. (2015). Robust constraints on average radial lower mantle anisotropy and consequences for composition and texture. *Earth and Planetary Science Letters*, *429*, 101–109. https://doi.org/10.1016/j.epsl.2015.07.057

Efron, B., & Tibshirani, R. (1986). Bootstrap methods for standard errors, confidence intervals, and other measures of statistical accuracy. *Statistical Science*, *1*, 54–75. https://doi.org/10.1214/ss/1177013815

Favier, N., & Chevrot, S. (2003). Sensitivity kernels for shear wave splitting in transverse isotropic media. *Geophysical Journal International*, *153*, 213–228. https://doi.org/10.1046/j.1365-246x.2003.01894.x

Fisher, N. I. (1995). *Statistical Analysis of Circular Data. Revised Edition*. New York, NY: Cambridge University Press.

Fouch, M. J., & Fischer, K. M. (1996). Mantle anisotropy beneath northwest Pacific subduction zones. *Journal of Geophysical Research*, *101*, 15,987–16,002. https://doi.org/10.1029/96JB00881

Gao, S., Davis, P. M., Liu, H., Slack, P. D., Rigor, A. W., Zorin, Y. A., et al. (1997). *SKS* splitting beneath continental rift zones. *Journal of Geophysical Research*, *102*, 22,781–22,797. https://doi.org/10.1029/97JB01858

Gao, S. S., & Liu, K. H. (2012). AnisDep: A FORTRAN program for the estimation of the depth of anisotropy using spatial coherency of shear-wave splitting parameters. *Computers & Geosciences*, *49*, 330–333. https://doi.org/10.1016/j.cageo.2012.01.020

Gao, S. S., & Liu, K. H. (2014). Mantle transition zone discontinuities beneath the contiguous United States. *Journal of Geophysical Research: Solid Earth*, *119*, 6452–6468. https://doi.org/10.1002/2014JB011253

Gao, S. S., Liu, K. H., & Abdelsalam, M. G. (2010). Seismic anisotropy beneath the Afar Depression and adjacent areas: Implications for mantle flow. *Journal of Geophysical Research*, *115*, B12330. https://doi.org/10.1029/2009JB007141

Girard, J., Amulele, G., Farla, R., Mohiuddin, A., & Karato, S. (2016). Shear deformation of bridgmanite and magnesiowustite aggregates at lower mantle conditions. *Science*, *351*, 144–147. https://doi.org/10.1126/science.aad3113

Hall, S. A., Kendall, J.-M., & van der Baan, M. (2004). Some comments on the effects of lower-mantle anisotropy on *SKS* and *SKKS* phases. *Physics of the Earth and Planetary Interiors*, *146*, 469–481. https://doi.org/10.1016/j.pepi.2004.05.002

Huang, Z., & Zhao, D. (2013). Mapping *P*-wave azimuthal anisotropy in the crust and upper mantle beneath the United States. *Physics of the Earth and Planetary Interiors*, *225*, 28–40. https://doi.org/10.1016/j.pepi.2013.10.003

Iidaka, T., & Niu, F. (1998). Evidence for an anisotropic lower mantle beneath eastern Asia: Comparison of shear-wave splitting data of *SKS* and P660s. *Geophysical Research Letters*, *25*, 675–678. https://doi.org/10.1029/98GL00297

James, D. E., & Assumpcao, M. (1996). Tectonic implications of *S*-wave anisotropy beneath SE Brazil. *Geophysical Journal International*, *126*, 1–10. https://doi.org/10.1111/j.1365-246x.1996.tb05263.x

Karato, S. (1998). Seismic anisotropy in the deep mantle, boundary layers and the geometry of mantle convection. *Pure and Applied Geophysics*, *151*, 565–587.

Karato, S., Zhang, S., & Wenk, H. R. (1995). Superplasticity in Earth's lower mantle: Evidence from seismic anisotropy and rock physics. *Science*, *270*, 458–461. https://doi.org/10.1126/science.270.5235.458

Kennett, B. L. N., & Engdahl, E. R. (1991). Traveltimes for global earthquake location and phase identification. *Geophysical Journal International*, *105*, 429–465. https://doi.org/10.1111/j.1365-246x.1991.tb06724.x

Kong, F., Gao, S. S., & Liu, K. H. (2015). On the applicability of the multiple-event stacking technique for shear-wave splitting analysis. *Bulletin of the Seismological Society of America*, *105*, 3156–3166. https://doi.org/10.1785/0120150078

Kong, F., Wu, J., Liu, K. H., & Gao, S. S. (2016). Crustal anisotropy and ductile flow beneath the eastern Tibetan Plateau and adjacent areas. *Earth and Planetary Science Letters*, *442*, 72–79. https://doi.org/10.1016/j.epsl.2016.03.003

Kosarev, G. L., Makeyeva, L. I., & Vinnik, L. (1984). Anisotropy of the mantle inferred from observations of *P* to *S* converted waves. *Geophysical Journal International*, *76*, 209–220. https://doi.org/10.1111/j.1365-246x.1984.tb05037.x

Li, Y., & Malin, P. E. (2008). San Andreas Fault damage at SAFOD viewed with fault-guided waves. *Geophysical Research Letters*, *35*, L08304. https://doi.org/10.1029/2007GL032924

Li, Z., & Peng, Z. (2017). Stress- and structure-induced anisotropy in Southern California from two decades of shear wave splitting measurements. *Geophysical Research Letters*, *44*, 9607–9614. https://doi.org/10.1002/2017GL075163

Lin, F., Ritzwoller, M. H., & Snieder, R. (2009). Eikonal tomography: Surface wave tomography by phase front tracking across a regional broad-band seismic array. *Geophysical Journal International*, *177*, 1091–1110. https://doi.org/10.1111/j.1365-246x.2009.04105.x

Lin, Y., Zhao, L., & Hung, S. (2014). Full-wave multiscale anisotropy tomography in Southern California. *Geophysical Research Letters*, *41*, 8809–8817. https://doi.org/10.1002/2014GL061855

Liu, H., Davis, P. M., & Gao, S. (1995). *SKS* splitting beneath Southern California. *Geophysical Research Letters*, *22*, 767–770. https://doi.org/10.1029/95GL00487

Liu, K. H., Elsheikh, A., Lemnifi, A., Purevsuren, U., Ray, M., Refayee, H., et al. (2014). A uniform database of teleseismic shear wave splitting measurements for the western and central United States. *Geochemistry, Geophysics, Geosystems*, *15*, 2075–2085. https://doi.org/10.1002/2014GC005267

Liu, K. H., & Gao, S. S. (2010). Spatial variations of crustal characteristics beneath the Hoggar swell, Algeria, revealed by systematic analyses of receiver functions from a single seismic station. *Geochemistry, Geophysics, Geosystems*, *11*, Q08011. https://doi.org/10.1029/2010GC003091

Liu, K. H., & Gao, S. S. (2011). Estimation of the depth of anisotropy using spatial coherency of shear-wave splitting parameters. *Bulletin of the Seismological Society of America*, *101*, 2153–2161. https://doi.org/10.1785/0120100258

Liu, K. H., & Gao, S. S. (2013). Making reliable shear-wave splitting measurements. *Bulletin of the Seismological Society of America*, *103*, 2680–2693. https://doi.org/10.1785/0120120355

Liu, K. H., Gao, S. S., Gao, Y., & Wu, J. (2008). Shear wave splitting and mantle flow associated with the deflected Pacific slab beneath northeast Asia. *Journal of Geophysical Research*, *113*, B01305. https://doi.org/10.1029/2007JB005178

Liu, H., & Niu, F. (2012). Estimating crustal seismic anisotropy with a joint analysis of radial and transverse receiver function data. *Geophysical Journal International*, *188*, 144–164. https://doi.org/10.1111/j.1365-246x.2011.05249.x

Long, M. D. (2009). Complex anisotropy in D″ beneath the eastern Pacific from *SKS-SKKS* splitting discrepancies. *Earth and Planetary Science Letters*, *283*, 181–189. https://doi.org/10.1016/j.epsl.2009.04.019

Long, M. D., & Silver, P. G. (2009). Shear wave splitting and mantle anisotropy: Measurements, interpretations, and new directions. *Surveys in Geophysics*, *30*, 407–461. https://doi.org/10.1007/s10712-009-9075-1

Lynner, C., & Long, M. D. (2012). Evaluating contributions to $SK(K)S$ splitting from lower mantle anisotropy: A case study from station DBIC, Cote D'Ivoire. *Bulletin of the Seismological Society of America*, *102*, 1030–1040. https://doi.org/10.1785/0120110255

Marson-Pidgeon, K., & Savage, M. K. (1997). Frequency-dependent anisotropy in Wellington, New Zealand. *Geophysical Research Letters*, *24*, 3297–3300. https://doi.org/10.1029/97GL03274

McNamara, D. E., Owens, T. J., Silver, P. G., & Wu, F. T. (1994). Shear wave anisotropy beneath the Tibetan plateau. *Journal of Geophysical Research*, *99*, 3,655–13,665. https://doi.org/10.1029/93JB03406

McNamara, A. K., van Keken, P. E., & Karato, S. (2002). Development of anisotropic structure in the Earth's lower mantle by solid-state convection. *Nature*, *416*, 310–314. https://doi.org/10.1038/416310a

Meade, C., Silver, P. G., & Kaneshima, S. (1995). Laboratory and seismological observations of lower mantle isotropy. *Geophysical Research Letters*, *22*, 1293–1296. https://doi.org/10.1029/95GL01091

Miller, V., & Savage, M. (2001). Changes in seismic anisotropy after volcanic eruptions: Evidence from Mount Ruapehu. *Science*, *293*, 2231–2233. https://doi.org/10.1126/science.1063463

Montagner, J. P., & Tanimoto, T. (1991). Global upper mantle tomography of seismic velocities and anisotropies. *Journal of Geophysical Research*, *96*, 20,337–20,351. https://doi.org/10.1029/91JB01890

Monteiller, V., & Chevrot, S. (2011). High-resolution imaging of the deep anisotropic structure of the San Andreas Fault system beneath Southern California. *Geophysical Journal International*, *186*, 418–446. https://doi.org/10.1111/j.1365-246x.2011.05082.x

Niu, F., & Perez, A. M. (2004). Seismic anisotropy in the lower mantle: A comparison of waveform splitting of *SKS* and *SKKS*. *Geophysical Research Letters*, *31*, L24612. https://doi.org/10.1029/2004GL021196

Ozalaybey, S., & Savage, M. K. (1995). Shear-wave splitting beneath western United States in relation to plate tectonics. *Journal of Geophysical Research*, *100*, 18,135–8,149. https://doi.org/10.1029/95JB00715

Porter, R., Zandt, G., & McQuarrie, N. (2011). Pervasive lower-crustal seismic anisotropy in Southern California: Evidence for underplated schists and active tectonics. *Lithosphere*, *3*, 201–220. https://doi.org/10.1130/L126.1

Press, W. H., Teukolsky, S. A., Vetterling, W. T., & Flannery, B. P. (1992). *Numerical recipes in FORTRAN, second edition*. Cambridge, UK: Cambridge University Press.

Restivo, A., & Helffrich, G. (2006). Core-mantle boundary structure investigated using *SKS* and *SKKS* polarization anomalies. *Geophysical Journal International*, *165*, 288–302. https://doi.org/10.1111/j.1365-246x.2006.02901.x

Romanowicz, B., & Wenk, H. (2017). Anisotropy in the deep Earth. *Physics of the Earth and Planetary Interiors*, *269*, 58–90. https://doi.org/10.1016/j.pepi.2017.05.005

Rumpker, G., Kaviani, A., & Latifi, K. (2014). *Ps*-splitting analysis for multilayered anisotropic media by azimuthal stacking and layer stripping. *Geophysical Journal International*, *199*, 146–163. https://doi.org/10.1093/gji/ggu154

Rumpker, G., & Ryberg, T. (2000). New "Fresnel-zone" estimates for shear-wave splitting observations from finite-difference modeling. *Geophysical Research Letters*, *27*, 2005–2008. https://doi.org/10.1029/2000GL011423

Rumpker, G., & Silver, P. G. (1998). Apparent shear-wave splitting parameters in the presence of vertically varying anisotropy. *Geophysical Journal International*, *135*, 790–800. https://doi.org/10.1046/j.1365-246x.1998.00660.x

Savage, M. K. (1999). Seismic anisotropy and mantle deformation: What have we learned from shear wave splitting? *Reviews of Geophysics*, *37*, 65–106. https://doi.org/10.1029/98RG02075

Savage, M. K., Peppin, W. A., & Vetter, U. R. (1990). Shear wave anisotropy and stress direction in and near Long Valley Caldera, California, 1979–1988. *Journal of Geophysical Research*, *95*, 11,165–11,177. https://doi.org/10.1029/JB095iB07p11165

Savage, M. K., & Silver, P. G. (1993). Mantle deformation and tectonics: Constraints from seismic anisotropy in the western United States. *Physics of the Earth and Planetary Interiors*, *78*, 207–227. https://doi.org/10.1016/0031-9201(93)90156-4

Schubert, G., Turcotte, D. L., & Olson, P. (2001). *Mantle Convection in the Earth and Planets*. Cambridge, UK: Cambridge University Press.

Schulte-Pelkum, V., & Mahan, K. H. (2014). A method for mapping crustal deformation and anisotropy with receiver functions and first results from USArray. *Earth and Planetary Science Letters*, *402*, 221–233. https://doi.org/10.1016/j.epsl.2014.01.050

Silver, P. G. (1996). Seismic anisotropy beneath the continents: Probing the depths of geology. *Annual Review of Earth and Planetary Sciences*, *24*, 385–432. https://doi.org/10.1146/annurev.earth.24.1.385

Silver, P. G., & Chan, W. W. (1991). Shear wave splitting and subcontinental mantle deformation. *Journal of Geophysical Research*, *96*, 16,429–16,454. https://doi.org/10.1029/91JB00899

Silver, P. G., & Savage, M. K. (1994). The interpretation of shear-wave splitting parameters in the presence of two anisotropic layers. *Geophysical Journal International*, *119*, 949–963. https://doi.org/10.1111/j.1365-246x.1994.tb04027.x

Tanimoto, T., & Anderson, D. L. (1984). Mapping convection in the mantle. *Geophysical Research Letters*, *11*, 287–290. https://doi.org/10.1029/GL011i004p00287

Tatham, D. J., Lloyd, G. E., Butler, R. W. H., & Casey, M. (2008). Amphibole and lower crustal seismic properties. *Earth and Planetary Science Letters*, *267*, 118–128. https://doi.org/10.1016/j.epsl.2007.11.042

Tong, C., Gudmundsson, O., & Kennett, B. L. N. (1994). Shear wave splitting in refracted waves returned from the upper mantle transition zone beneath northern Australia. *Journal of Geophysical Research*, *99*, 15,783–15,797. https://doi.org/10.1029/94JB00460

Vinnik, L., & Montagner, J. P. (1996). Shear wave splitting in the mantle *Ps* phases. *Geophysical Research Letters*, *23*, 2449–2452. https://doi.org/10.1029/96GL02263

Wei, W., Zhao, D., Xu, J., Zhou, B., & Shi, Y. (2016). Depth variations of *P*-wave azimuthal anisotropy beneath Mainland China. *Scientific Reports*, *6*, 29614. https://doi.org/10.1038/srep29614

Wolfe, C. J., & Silver, P. G. (1998). Seismic anisotropy of oceanic upper mantle: Shear wave splitting methodologies and observations. *Journal of Geophysical Research*, *103*, 749–771. https://doi.org/10.1029/97JB02023

Wu, J., Zhang, Z., Kong, F., Yang, B. B., Yu, Y., Liu, K. H., & Gao, S. S. (2015). Complex seismic anisotropy beneath western Tibet and its geodynamic implications. *Earth and Planetary Science Letters*, *413*, 167–175. https://doi.org/10.1016/j.epsl.2015.01.002

Yang, B. B., Liu, K. H., Dahm, H. H., & Gao, S. S. (2016). A uniform database of teleseismic shear wave splitting measurements for the western and central United States: December 2014 update. *Seismological Research Letters*, *87*, 295–300. https://doi.org/10.1785/0220150213

Yang, B. B., Liu, Y., Dahm, H., Liu, K. H., & Gao, S. S. (2017). Seismic azimuthal anisotropy beneath the eastern United States and its geodynamic implications. *Geophysical Research Letters*, *44*, 2670–2678. https://doi.org/10.1002/2016GL071227

Yang, Z., Sheehan, A., & Shearer, P. (2011). Stress-induced upper crustal anisotropy in Southern California. *Journal of Geophysical Research*, *116*, B02302. https://doi.org/10.1029/2010JB007655

Zhang, S., & Karato, S. (1995). Lattice preferred orientation of olivine aggregates deformed in simple shear. *Nature*, *375*, 774–777. https://doi.org/10.1038/375774a0